Towards Holographic Antenna Systems for MIMO Radar and Communication Applications

Thomas Frey*, Maximilian Döring, Christian Waldschmidt, Tobias Chaloun
*University Ulm, Institute of Microwave Engineering, 89081 Ulm, Germany
Email: thomas.frey@uni-ulm.de

***Abstract*—A novel synthesis method using an incident angle dependent impedance mapping for holographic multi-feed antennas is presented. Since the unit cells of the holographic antenna are shared with all feeds, it is necessary to merge all of the sub-holograms to a common physical geometry. In the proposed multi-beam synthesis, a individual merged impedance hologram for each feeding point is determined, which has the lowest impedance error to the corresponding analytical holograms. Subsequently, a non pixel-based genetic optimization is used to account for global error minimization across all feeds. The antenna is going to be realized on glass due its lower loss and dispersive properties compared to Teflon-based materials at mm-wave frequencies. In addition to the incident angle dependent hologram synthesis method, an appropriate sub-wavelength pixel has been design and optimized with enhanced anisotropic properties. The implemented holographic multi-feed antenna design has an antenna gain of 23.3 dBi and 23.0 dBi, a polarization purity of 20.3 dB and 23.0 dB and a side-lobe level of −18.5 dB and −19.0 dB with 2 feeds at 77 GHz.**

***Index Terms*—multi-feed antenna, holographic antenna, metasurface antenna, multiple-input−multiple-output (MIMO), glass technology, high-gain.**

I. Introduction

Holographic antennas enable a highly flexible control of the objective field distribution in both amplitude and phase [1], [2]. This can be achieved by an impedance hologram, whose transverse modulation period controls the phase distribution to synthesize a desired beam pattern. In order to integrate a holographic antenna on a multiple-input−multiple-output (MIMO) radar, it is necessary that the antenna have multiple feeding points. However, only the realization of a single pixel geometry within a unit cell (UC) is possible. This requires a superposition of all holograms and their pixel geometries of each individual feed.

In recently published contributions the hologram superposition is implemented by a pixel-based arithmetic averaging of all individual impedance tensor holograms concerning each feeding point [3], [4], [5]. The incident angular dependency of the surface-wave (SW) w.r.t. the unit cell does not taking into account on those design methodologies, which lead to an increased discrepancy of the merged impedance hologram to the individual analytical holograms.

In this paper, a novel synthesis process for holographic multi-feed antennas by an incident angle dependent impedance mapping is presented. Instead of superimposing all impedance holograms into a common one, an individual hologram is determined for each feeding point depending on its incident angle w.r.t. the UC. This minimizes the absolute impedance error of each feed to its corresponding analytical hologram. For further improvement of the radiation pattern and additional minimization of the global impedance error, a non pixel-based genetic optimization is performed.

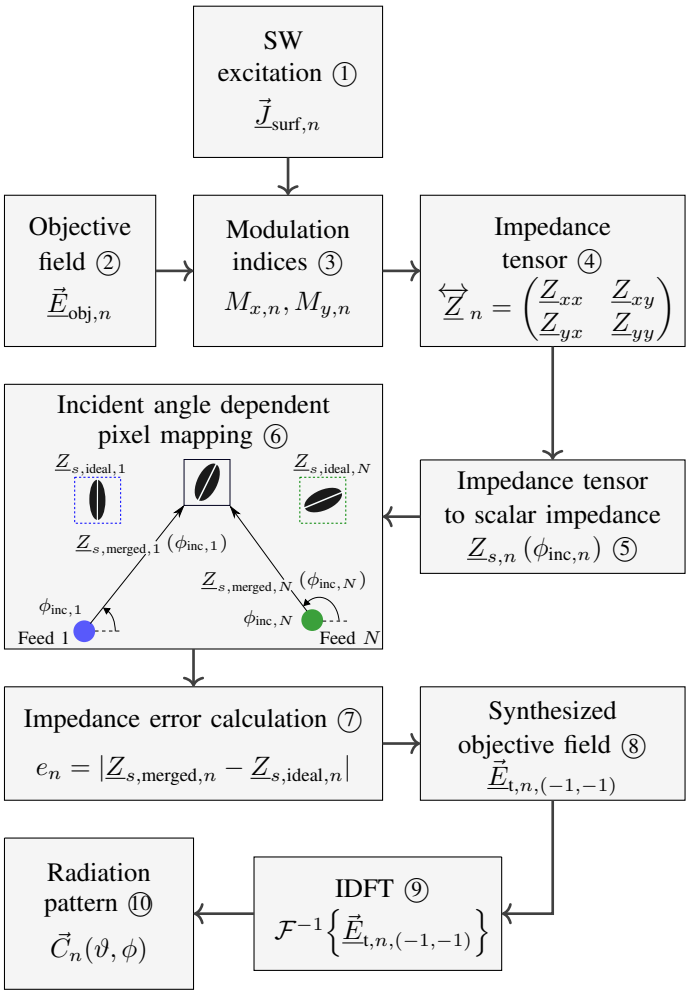

Fig. 1: Design and analytical synthesis process of the holographic multi-feed antenna having N independent feeding points.

II. Multi-feed Synthesis

The proposed design and analytical synthesis process for holographic multi-feed antennas having N feeds is depicted in Fig. 1. For a leaky-wave (LW) radiation, a SW needs to be stimulated by each single feed source. For this purpose, each feed n excites a TM_0 SW propagating on the antenna aperture and with a current distribution $\underline{J}_{\mathrm{surf},n}$ (see ① in Fig. 1). The desired objective field distribution to be synthesized possesses the form (see ② in Fig. 1)

$$\underline{\vec{E}}_{\mathrm{obj},n} = \begin{pmatrix} E_{x_0,n}\mathrm{e}^{-\mathrm{j}(k_{x,n}x)}\, T_{x,n}\,(x,y) \\ E_{y_0,n}\mathrm{e}^{-\mathrm{j}\left(k_{y,n}y \mp \frac{\pi}{2}\right)}\, T_{y,n}\,(x,y) \end{pmatrix} \quad \forall\, n \in \mathbb{N}\,, \tag{1}$$

where $T_{x,n}$ and $T_{y,n}$ are the x- and y-components of the desired amplitude taper function $\vec{T}_n\,(x,y)$ of the n-th feeding point. The phase expressions are set to synthesize a circularly polarized electric field, whose constant amplitudes are described by $E_{x_0,n}$ and $E_{y_0,n}$.

To synthesize the objective electric field from (1), the excited SW has to interact with a periodic structure of sub-wavelength discontinuities, which are described by the anisotropic surface impedance tensor hologram $\overleftrightarrow{\underline{Z}}_n$ (see ④ in Fig. 1). The synthesis results in an individual tensor hologram for each of the n feeds. However, only one single physical realization on the antenna aperture is possible and therefore, a superposition of all N impedance tensor holograms must take place (see ⑥ in Fig. 1). The synthesized objective field distribution of the n-th feeding point (see ⑧ in Fig. 1) is defined by $\underline{\vec{E}}_{\mathrm{t},n,(-1,-1)}$ and contains the electric field distribution of the $(-1,-1)$ LW mode, whose Fourier spectrum is related to the far field pattern of the holographic multi-feed antenna (see ⑩ in Fig. 1). Hence, each feed generates its own individual far field pattern. The space-dependent modulation indices $M_{x,n}$ and $M_{y,n}$ provide a specified configuration of the far field pattern regarding the 3-dB-beamwidth and the side lobe level (SLL) for each feeding point n

$$M_{x,n} = \left| \frac{\underline{\vec{E}}_{\mathrm{obj},x,n}}{\underline{\vec{E}}_{\mathrm{t,avg},n}} \right| \quad , \quad M_{y,n} = \left| \frac{\underline{\vec{E}}_{\mathrm{obj},y,n}}{\underline{\vec{E}}_{\mathrm{t,avg},n}} \right| . \tag{2}$$

III. Multi-feed Hologram Pixel Mapping

The theoretical impedance hologram can be obtained from the analytical antenna model from Sec. II. For the realization of these anisotropic surface impedances, a pixel modeling is necessary. The unit cell (UC) dimension is small compared to the wavelength ($\approx \lambda_0/10$) to obtain a homogeneous impedance assumption. The variation of the impedance is achieved by changing the geometrical parameters of the pixel, which is located in the center of the UC. Due to the fact that only one physical pixel for every UC can be realized on the antenna aperture, an appropriate superposition of all N individual surface impedance holograms must be realized at the same time.

A. State of the art - arithmetic impedance averaging

In recently published contributions, the hologram superposition is implemented by a pixel-based arithmetic averaging of all N impedance tensor holograms $\overleftrightarrow{\underline{Z}}_n\,(i)$ to a common one [3], [4], [5]:

$$\overleftrightarrow{\underline{Z}}_{\mathrm{merged}}\,(i) = \frac{1}{N}\sum_{n=1}^{N} \overleftrightarrow{\underline{Z}}_n\,(i) \qquad \forall i \wedge n \in \mathbb{N}\,. \tag{3}$$

However, those design methodologies do not take the angular dependency of the unit cell surface impedance into account. Since an averaging of the tensor is performed, this physically corresponds to an arithmetic averaging of the N individual pixel geometries for each feeding point. This results in the absolute impedance error matrix

$$\overleftrightarrow{e}\,(i) = \left| \left(\sum_{n=1}^{N} \overleftrightarrow{\underline{Z}}_{\mathrm{ideal},n}\,(i) \right) - N\,\overleftrightarrow{\underline{Z}}_{\mathrm{merged}}\,(i) \right| \quad \forall\, i \wedge n \in \mathbb{N}\,, \tag{5}$$

of the superimposed hologram $\overleftrightarrow{\underline{Z}}_{\mathrm{merged}}\,(i)$ to each n-th individual hologram $\overleftrightarrow{\underline{Z}}_{\mathrm{ideal},n}\,(i)$, which results from the analytical calculation (see ⑦ in Fig. 1). The impedance error is used as an evaluation criterion for the correctness of the merged pixel geometry for each UC of the holographic multi-feed antenna.

B. Preliminary consideration of the anisotropic impedance tensor mapping

From the analytical antenna model an impedance tensor for each unit cell is obtained (see ④ in Fig. 1). Therefore, a complex eigenvalue problem has to be solved, which depends on the incident angle ϕ_{inc} of the SW on the UC and resulting in an impenetrable scalar surface impedance $\underline{Z}_{\mathrm{s}}\,(\phi_{\mathrm{inc}})$. For

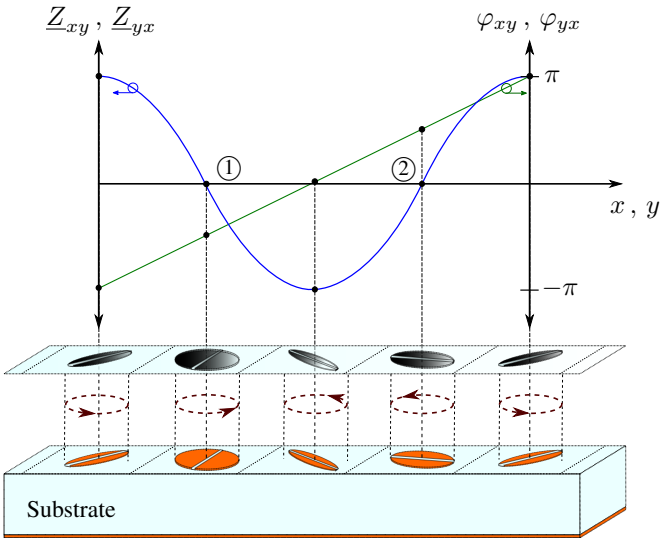

Fig. 2: Unambiguous assignment of the anisotropy of a 2π-periodic pixel structure by means of the amplitude (—) and phase information (—) of the anisotropic components of the impedance tensor for their physical realization.

$$\underline{Z}_s\left(\phi_{\text{inc}}\right) = Z_{\text{F0}}\cdot\Bigg[-\text{j}\left(Z_{\text{F0}}^2 - \underline{Z}_{xy}\underline{Z}_{yx} + \underline{Z}_{xx}\underline{Z}_{yy}\right) \pm \Bigg[-\left(Z_{\text{F0}}^2 - \underline{Z}_{xy}\underline{Z}_{yx} + \underline{Z}_{xx}\underline{Z}_{yy}\right)^2 + 4Z_{\text{F0}}^2\cdot\left(\underline{Z}_{xx}\sin^2\left(\phi_{\text{inc}}\right) - \frac{1}{2}\left(\underline{Z}_{xy} + \underline{Z}_{yx}\right)\sin\left(2\phi_{\text{inc}}\right) + \underline{Z}_{yy}\cos^2\left(\phi_{\text{inc}}\right)\right)\cdot\left(\underline{Z}_{xx}\cos^2\left(\phi_{\text{inc}}\right) - \frac{1}{2}\left(\underline{Z}_{xy} + \underline{Z}_{yx}\right)\sin\left(2\phi_{\text{inc}}\right) + \underline{Z}_{yy}\sin^2\left(\phi_{\text{inc}}\right)\right)\Bigg]^{\frac{1}{2}}\Bigg]\cdot\left[2Z_{\text{F0}}\left(\underline{Z}_{xx}\sin^2\left(\phi_{\text{inc}}\right) - \frac{1}{2}\left(\underline{Z}_{xy} + \underline{Z}_{yx}\right)\sin\left(2\phi_{\text{inc}}\right) + \underline{Z}_{yy}\cos^2\left(\phi_{\text{inc}}\right)\right)\right]^{-1} \tag{4}$$

a meaningful assignment of the given analytical impedance tensor $\underline{\overleftrightarrow{Z}}_{\text{ideal},n}$ to a physical pixel geometry, the calculation of its corresponding analytical scalar surface impedance is necessary (see ⑤ in Fig. 1). Solving (16) from [6] for k_z/k_0 under the condition $\underline{Z}_{xy} \neq \underline{Z}_{yx}$, the analytic scalar surface impedance for each UC results in (4), where $\underline{Z}_{xy}$, $\underline{Z}_{yx}$ are the anisotropic and $\underline{Z}_{xx}$, $\underline{Z}_{yy}$ are the isotropic tensor entries, k_z is the wavenumber in z-direction, and k_0 is the free-space wavenumber. The free-space impedance is expressed by Z_{F0} and ϕ_{inc} equals the incident angle of the SW w.r.t. the UC (see ⑥ in Fig. 1). A method to control the surface currents in every direction and to realize the anisotropic impedance tensor is to insert a slot through the center of a pixel geometry, where the slot has an orientation angle ϕ_{slot} (see Fig. 2). Since no unambiguous slot orientation can be assigned to the course of the scalar impedance on the antenna aperture, the anisotropic components are used in this novel synthesis process. The amplitude curve (—) and phase progression (—) of $\underline{Z}_{xy}$ or $\underline{Z}_{yx}$ are depicted in Fig. 2. The amplitude does not allow a clear assignment of the anisotropic degree to a unambiguous slot angle within a 2π-period as depicted in Fig. 2. For instance at the intersections ① and ②, the same amplitudes but different slot angles of 90° and 0° are present. Therefore, only the phase progression of the anisotropic tensor components offers an unambiguous assignment between the slot angle and the anisotropic intensity (c.f. Fig. 2)

$$\varphi_{xy}\left(x,y\right) = \beta_{\text{SW}}\sqrt{x^2+y^2} - \left(k_x x + k_y y\right) + \phi_{\text{inc}}\,, \tag{6}$$

where $\varphi_{xy} = \varphi_{xy}$, β_{SW} is the SW phase constant, and k_x/k_y are the wavenumbers in the x- and y-direction, respectively. These impedance values and the corresponding dimensions of the pixel are stored in a database as a look-up table. As a result, every UC has an assigned slot orientation due to its anisotropic tensor components. Subsequently, the geometric parameters, which yields to the lowest impedance error (see (5)), determines the scalar impedance as function of the incident angle $\phi_{\text{inc},n}$ (see ⑦ in Fig. 1). This results in an unambiguous pixel geometry for the scalar impedance and its corresponding impedance tensor.

C. Incident angle dependent impedance mapping

To overcome this problem from Sec. III-A, a novel synthesis process for holographic multi-feed antennas is presented. Since only a single physical pixel geometry realization in a UC is possible, it is necessary to merge all the N individual pixel geometries of each n-th hologram. The holograms are not averaged to a common one, but a merged hologram, depending on the incident angle, for each n-th feed is determined to minimize the impedance error to its corresponding analytical hologram. As the incident angle of each feed w.r.t. the individual UC is considered, N scalar impedance values are obtained from a single pixel geometry with the minimum impedance error for each UC (see ⑥ in Fig. 1). The N individual analytic scalar impedances of the holograms

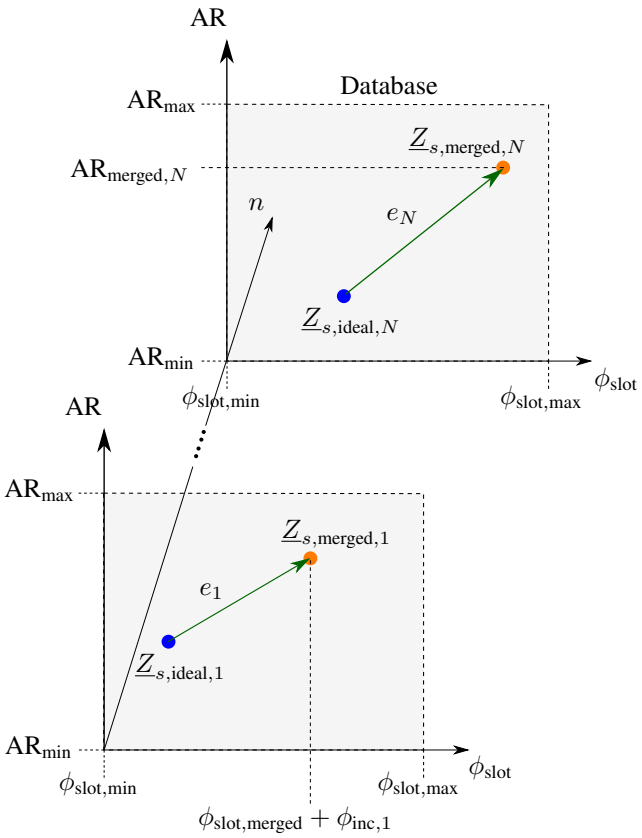

Fig. 3: Illustration of the incident angle dependent pixel mapping (see ⑥ in Fig. 1) to find the merged pixel geometry $\text{AR}_{\text{merged}}$ and $\phi_{\text{slot,merged}}$ for the minimum impedance error.

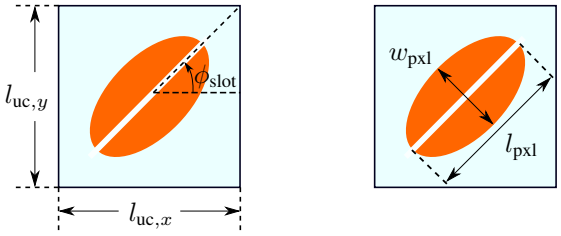

Fig. 4: Elliptical 2π-periodic pixel structure with an additional slot through the center within the unit cell.

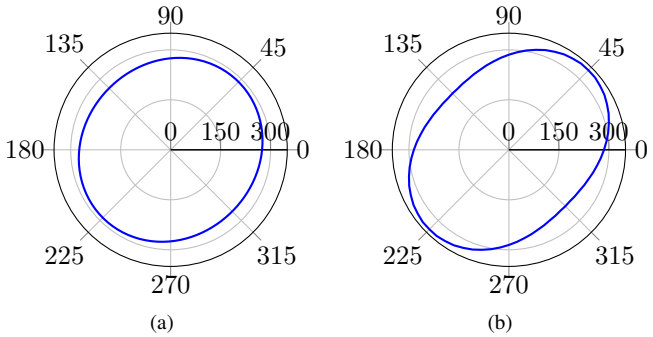

Fig. 5: Scalar impedance of (a) a circular pixel with slot and (b) an elliptical pixel with slot over the incident angle range $\phi_{\mathrm{inc}} = [0°, 360°]$ at the fixed slot angle $\phi_{\mathrm{slot}} = 45°$ at 77 GHz.

(see (4)) are defined by its corresponding slot angle $\phi_{\mathrm{slot,ideal},n}$ (as described in Sec. III-B) and its aspect ratio (AR) for each UC as depicted in Fig. 4. The AR is defined as

$$\mathrm{AR} = \frac{w_{\mathrm{pxl}}}{l_{\mathrm{pxl}}} \qquad \forall\ \mathrm{AR} \in]0, 1]. \tag{7}$$

Thus, a merged slot angle $\phi_{\mathrm{slot,merged}}$ and a merged aspect ratio $\mathrm{AR}_{\mathrm{merged}}$ with a minimum error regarding the N ideal geometry values of each feed must be found for every UC. After determining the merged slot angle $\phi_{\mathrm{slot,merged}}$, the incident angle of each feed n on the considered UC $\phi_{\mathrm{inc},n}$ is included. A database matrix look-up table (LUT) is created for this purpose, containing all scalar impedance values $\underline{\mathbf{Z}}_{s,\mathrm{LUT}}$ for L different aspect ratios (see (7)) and M slot angels (see Fig. 3). Subsequently, the goal is to find the minimum impedance error of the N different scalar impedance values $\underline{Z}_{s,\mathrm{merged},n}$, which depend on the incident angle, in comparison to the individual ideal analytic impedances $\underline{Z}_{s,\mathrm{ideal},n}$ to find the same AR ($\mathrm{AR}_{\mathrm{merged}}$). Thereby $\underline{\mathbf{Z}}_{s,\mathrm{LUT}}$ is a line vector for each n-th direction dependent slot angle $\phi_{\mathrm{slot,merged}} + \phi_{\mathrm{inc},n}$ and contains all scalar impedance values as a function of the AR

$$\mathrm{AR}_{\mathrm{merged}}(i) = \min\left[\sum_{n=1}^{N}\left|\underline{\mathbf{Z}}_{s,\mathrm{LUT}}(\phi_{\mathrm{slot,merged}} + \phi_{\mathrm{inc},n}, \mathrm{AR}) - \underline{Z}_{s,\mathrm{ideal},n}(i)\right|\right] \quad \forall\, i \wedge n \in \mathbb{N}. \tag{8}$$

This results in an $N \times L$ error matrix, where the sum within a column is formed to determine the lowest impedance error and to find the merged AR (see Fig. 3). The absolute scalar impedance error $e(i)$ for each i-th unit cell is given by (see ⑦ in Fig. 1)

$$e(i) = \sum_{n=1}^{N}\left|\underline{Z}_{s,\mathrm{ideal},n}(i) - \underline{Z}_{s,\mathrm{merged},n}(i)\right| \quad \forall\, i \wedge n \in \mathbb{N}. \tag{9}$$

Thus, the N scalar impedances $\underline{Z}_{s,\mathrm{merged},n}$ of the merged pixel geometry are a function of the AR and the slot angle

$$\underline{Z}_{s,\mathrm{merged},n}(i)\,(\phi_{\mathrm{slot,merged}}(i) + \phi_{\mathrm{inc},n}(i), \mathrm{AR}_{\mathrm{merged}}(i)) \tag{10}$$

refereed to each individual incident angle of the n-th feed SW w.r.t the i-th unit cell (c.f. ⑥ in Fig. 1).

D. Anisotropic pixel optimization

The conventional anisotropic 2π-periodic pixel structure consists of a circle shaped patch with additional slot through its center to realize an anisotropic impedance tensor [2]. However, these pixel geometry can be improved in terms of anisotropy. Therefore, an extension of the elliptical pixel shape with an additional slot is realized. Thus, the current will tend to run along the direction of the ellipse and additionally along the slot resulting in an increased portion in the TE-component of the TM-TE-hybrid LW mode. Figure 5(a) shows the scalar impedance of a circular pixel with additional slot over the incident angle for the pixel width $w_{\mathrm{pxl}} = 275\,\mu\mathrm{m}$ and Fig. 5(b) shows the scalar impedance of an elliptical pixel with additional slot over the incident angle for the aspect ratio $\mathrm{AR} = 0.5$. The elliptical pixel with slot shows an increased peanut-shaped course of the scalar impedance indicating an enhanced anisotropy degree.

IV. Realization and Measurement

A. Design process

Based on the synthesis process discussed in Sec. II, a holographic multi-feed antenna is designed. The thickness of the glass wafer is set to $400\,\mu\mathrm{m}$ in order to suppress higher order SW modes. The antenna has two feeding points at $(x_1 = -2\,\mathrm{mm},\ y_1 = -7.8\,\mathrm{mm})$ and $(x_2 = -0.2\,\mathrm{mm},\ y_2 = 3\,\mathrm{mm})$ calculated by a non pixel-based genetic optimization with respect to the lowest impedance error (9). Two coplanar waveguides (CPW) within the ground metallization are used to feed the surface wave launchers from the bottom side. The dimensions of the CPW feeding correspond to the characteristic impedance of $50\,\Omega$. The antenna consists of 10000 squared UCs. To ensure a homogeneous periodic structure, the UC size is set to $0.4\,\mathrm{mm} \times 0.4\,\mathrm{mm}$. This results in an antenna aperture dimension of $40\,\mathrm{mm} \times 40\,\mathrm{mm}$. Due to the increased anisotropy (Sec. III-D), the UC geometry is based on an elliptical shaped metal patch with an inclined slot to produce anisotropic impedance tensors (see Fig. 4). The orientation of the ellipse and the slot is determined by the anisotropic

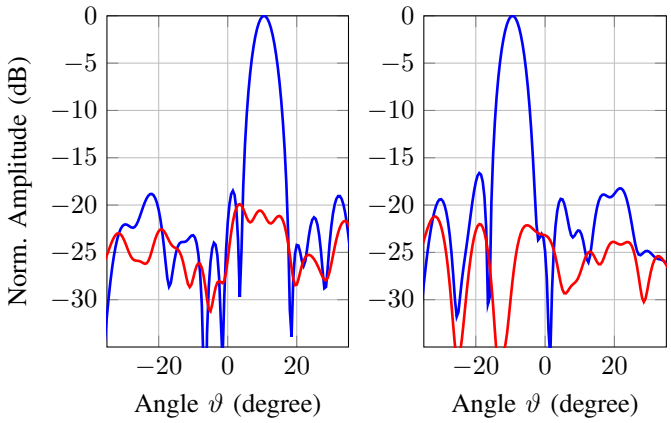

(a) Feed 1: Azimth cut at $\phi_0 = 0°$. (b) Feed 2: Azimth cut at $\phi_0 = 0°$.

Fig. 6: Simulated radiation patterns of the holographic multi-feed antenna on glass at 77 GHz.

tensor components to enhance the polarization purity. These UC dimensions and the pixel geometry provide a maximum modulation index of $\max\{M_{x,y}\} = 0.181$ and an average impedance of $\underline{Z}_{\text{avg}} = \text{j}328.9\,\Omega$ for each feed. The designed holographic multi-feed antenna is intended to radiate a single beam for each feed in the azimuth direction and is tilted to an elevation angle of $\vartheta_{0,1} = 10°$ and $\vartheta_{0,2} = -10°$ at 77 GHz.

B. Simulation and analysis

The simulation model of the optimized holographic multi-feed antenna on glass was constructed on a fused silica substrate with a relative permittivity $\varepsilon_r = 3.78$ and a dielectric loss factor $\tan\delta = 0.001$. The metallization for the periodic pixel structures and the ground plane consists of a 10 nm thick chromium seed layer, on which a 350 nm gold layer is added. The individual pixel structures is going to be realized by a conventional wet etching process with tolerances of $\pm 2\,\mu\text{m}$. A probe tip in upside-down orientation is used to feed the proposed holographic antenna on glass from the bottom side in order to avoid the parasitic impact of the probe on the radiation pattern of the antenna under test (AUT) [7]. The far field simulations of the modeled holographic multi-feed antenna are conducted using a full wave simulation tool. In Fig. 6 the full wave simulated radiation patterns of both feeds of the holographic antenna are illustrated for elevation angles in the range $\pm 35°$ at 77 GHz at the azimuth angle 0°. A gain for feed 1 and feed 2 of 23.3 dBi and 23.0 dBi and a polarization purity of 20.3 dB and 23.0 dB were simulated. A minimum side lobe level of -18.5 dB, a 3-dB-beamwidth of 6° and a minimum reflection coefficient of -13 dB were simulated at 77 GHz. The calculated directivity based on the 3D-radiation pattern simulation results is 23.5 dBi and 23.2 dBi at 77 GHz resulting in a radiation efficiency of 95 %. The measurement results will be presented at the conference.

V. Conclusion

In this paper, a novel synthesis process using an incident angle dependent impedance mapping for holographic multi-feed antennas is presented. Therefore, a merged hologram for each feed n is determined, which has the lowest impedance error to the corresponding analytical holograms optimized by an non pixel-based genetic algorithm. The antenna design was realized with two feeds towards an automotive mm-wave MIMO-Radar application. By using the glass technology, a low-loss multi-feed antenna with a very high radiation efficiency of 95 % can be realized. The far field simulations prove the high-quality radiation pattern concerning both feeding points at the operation frequency of 77 GHz. Furthermore, a novel pixel geometry regarding an optimization of the anisotropy was introduced and evaluated. The simulated radiation patterns show an antenna gain of 23.3 dBi and 23.0 dBi, a polarization purity of 20.3 dB and 23.0 dB and a side-lobe level of -18.5 dB and -19.0 dB.

Acknowledgment

This work was supported by the German Federal Ministry of Education and Research (BMBF) and the Federal States of Germany Grant “Innovative Hochschule” (FKZ) 03IHS024D. The authors would like to thank LPKF Laser & Electronics AG for processing and machining the glass wafer to realize the holographic multifeed antenna prototype.

References

[1] G. Minatti, F. Caminita, M. Casaletti, and S. Maci, “Spiral Leaky-Wave Antennas Based on Modulated Surface Impedance,” *IEEE Transactions on Antennas and Propagation*, vol. 59, no. 12, pp. 4436–4444, Dec. 2011.

[2] G. Minatti, F. Caminita, E. Martini, M. Sabbadini, and S. Maci, “Synthesis of Modulated-Metasurface Antennas With Amplitude, Phase, and Polarization Control,” *IEEE Transactions on Antennas and Propagation*, vol. 64, no. 9, pp. 3907–3919, 2016.

[3] D. González-Ovejero, G. Minatti, G. Chattopadhyay, and S. Maci, “Multibeam by Metasurface Antennas,” *IEEE Transactions on Antennas and Propagation*, vol. 65, no. 6, pp. 2923–2930, Jun. 2017.

[4] D. Gonzalez-Ovejero, G. Minatti, E. Martini, G. Chattopadhyay, and S. Maci, “Shared Aperture Metasurface Antennas for Multibeam Patterns,” in *11th European Conference on Antennas and Propagation (EUCAP)*, pp. 3332–3335.

[5] D. G. Ovejero, G. Minatti, M. Faenzi, F. Caminita, E. Martini, and S. Maci, “Shared-Aperture Modulated Metasurface Antennas,” in *XXXIInd General Assembly and Scientific Symposium of the International Union of Radio Science (URSI GASS)*, pp. 1–3.

[6] B. H. Fong, J. S. Colburn, J. J. Ottusch, J. L. Visher, and D. F. Sievenpiper, “Scalar and Tensor Holographic Artificial Impedance Surfaces,” *IEEE Transactions on Antennas and Propagation*, vol. 58, no. 10, pp. 3212–3221, Oct. 2010.

[7] T. Galler, T. Frey, C. Waldschmidt, and T. Chaloun, “High-Gain Millimeter-Wave Holographic Antenna in Package using Glass Technology,” *IEEE Antennas and Wireless Propagation Letters*, pp. 1–5, 2020.

[8] L. Boehm, F. Boegelsack, M. Hitzler, and C. Waldschmidt, “The Challenges of Measuring Integrated Antennas at Millimeter-Wave Frequencies [Measurements Corner],” *IEEE Antennas and Propagation Magazine*, vol. 59, no. 4, pp. 84–92, Aug. 2017.